

Low-loss multilevel operation using lossy phase-change material-integrated silicon photonics

Rui Chen¹,^{a,*} Virat Tara,^a Jayita Dutta¹,^a Zhuoran Fang,^a Jiajiu Zheng¹,^a and Arka Majumdar¹,^{a,b,*}

^aUniversity of Washington, Department of Electrical and Computer Engineering, Seattle, Washington, United States

^bUniversity of Washington, Department of Physics, Seattle, Washington, United States

ABSTRACT. Chalcogenide phase-change materials (PCMs) offer paradigms for programmable photonic integrated circuits thanks to their zero static energy and significant refractive index contrast. However, prototypical PCMs, such as $\text{Ge}_2\text{Sb}_2\text{Te}_5$ (GST), are lossy in their crystalline phase, albeit transparent in the amorphous state. Moreover, electrically switching PCMs to intermediate states is a stochastic process, limiting programming accuracy. As a result, achieving both low-loss and deterministic multilevel operations with GST remains challenging. Although low-loss PCMs, such as Sb_2S_3 and Sb_2Se_3 , have been discovered in recent years, they are much less technologically mature. We propose a design with multiple GST segments to overcome the challenge of deterministic multilevel operation. GST segments are individually controlled by interleaved silicon p++-doped-intrinsic-n+-doped diode heaters in a binary but reliable fashion, and multiple levels are encoded in their phase sequence. A 1×1 programmable unit with two unequal GST segments is experimentally demonstrated, showcasing four distinct operation levels and negligible thermal crosstalk with only one pair of metal contacts. We then extend the design to 1×2 and 2×2 programmable units. For the 2×2 programmable unit design, we propose a phase-detuned three-waveguide directional coupler structure to mitigate the absorption and radiation loss, showing <1.2 dB loss and three splitting ratios. We provide a new path toward low-loss and multilevel optical switches using lossy PCMs.

© The Authors. Published by SPIE under a Creative Commons Attribution 4.0 International License. Distribution or reproduction of this work in whole or in part requires full attribution of the original publication, including its DOI. [DOI: [10.1117/1.JOM.4.3.031202](https://doi.org/10.1117/1.JOM.4.3.031202)]

Keywords: phase-change materials; optical programmable units; multilevel electrical control; phase-detuned directional couplers

Paper 24004SS received Feb. 13, 2024; revised Mar. 19, 2024; accepted Mar. 21, 2024; published Jun. 13, 2024.

1 Introduction

Programmable photonic integrated circuits (PICs), consisting of meshes of tunable beam splitters and/or optical phase shifters,¹ are extending their applications from widely used optical communication to optical computing,² microwave photonics,³ and quantum information processing.^{4,5} To further scale up the programmable PICs, it is necessary to achieve low-loss, low-crosstalk, compact, low-power-consumption, multilevel programmable units. However, most programmable PICs utilize weak and volatile tuning mechanisms such as thermo-optic,^{6,7}

*Address all correspondence to Rui Chen, charey@uw.edu; Arka Majumdar, arka@uw.edu

electro-optics,⁸ or free-carrier effects,⁹ providing very small and volatile refractive index change ($\Delta n < 0.01$). As a result, the devices usually have a large footprint ($> 100 \mu\text{m}$ ¹⁰) and require a constant power supply ($\sim 10 \text{ mW}$), incurring limited density and energy efficiency.

Nonvolatile chalcogenide phase-change materials (PCMs)^{11–14} are a very promising platform. These materials have two stable microstructural phases in the ambient environment, i.e., the thermodynamically favorable crystalline (c) phase and metastable amorphous (a) phase. Due to the change in atomic arrangement, a and c phases differ significantly in their refractive index ($\Delta n \sim 1$). Earlier experiments have shown that the phases can be controlled both optically using pulsed lasers^{15–18} and electrically via on-chip microheaters.^{19–23} It is worth noting that since both phases are stable, zero power is needed to maintain the state once the PCM phase is changed. In addition, this memory effect can reduce the complexity of control circuits as electronic memory blocks and time-division multiplexing are avoided. The large Δn and nonvolatility together offer compact devices ($\sim 10 \mu\text{m}$ ^{23,24}) with zero static energy consumption, hence a unique opportunity to achieve ultra-low-power programmable PICs.

Most technologically mature PCMs, such as $\text{Ge}_2\text{Sb}_2\text{Te}_5$ (GST) and GeTe, are very lossy in the c phase particularly in the near-infrared regime ($\sim 1550 \text{ nm}$), although they are transparent in the a phase. In spite of the emergence of wide bandgap PCMs, such as Sb_2S_3 and Sb_2Se_3 ,^{21–23,25–28} they are much less understood and therefore are less likely to be integrated in large-scale foundry processes. In this work, we consider the prototypical PCM GST, which has been widely used for electronic memory applications^{29,30} and holds promise to integrate into the photonic foundries. As explained earlier, one major limitation of GST at 1550 nm is the absorption loss of c-GST, which prohibits it from phase-only modulation as needed for large-scale switching fabrics³¹ or interferometry-based optical signal processors.² To mitigate the loss, a phase-matched three-waveguide directional coupler (PM-TDC) design was reported in previous studies.^{20,24,31} In addition to the loss, deterministic multilevel operation also remains challenging. Although pulse width or amplitude modulation^{22,23} could produce mixed a and c phases, thereby having multiple operation levels, such a process is inherently stochastic.³² Furthermore, these schemes cannot be used in the PM-TDC design, which causes a large loss due to either material absorption or radiation loss at the end of the transition waveguide (WG).

In this work, we propose and numerically demonstrate low-loss optical programmable units based on a lossy PCM GST, including 1×1 , 1×2 , and 2×2 programmable units. Our devices support deterministic multilevel operation with individually controlled GST segments, which are controlled by a series of interleaved p++-doped-intrinsic-n++-doped (PIN) silicon microheaters. Each microheater controls the corresponding segment in a binary way, and different states can be achieved by programming the phases of the GST segments. We emphasize that this scheme is inherently deterministic compared with engineering the electrical pulse amplitude,²² duration, or number of pulses,²¹ as it solely relies on the binary phase transition, which is more deterministic than achieving intermediate states. We show that 1×1 and 1×2 programmable units can achieve multiple operation levels using segmented PCM. We reported two methods to achieve 2^N and $(N + 1)$ states with N segments. A preliminary experiment on 1×1 WG programmable units with the segmented GST shows distinct multiple operation levels without significant thermal crosstalk. The rectified property of PIN diode heaters was exploited in this programmable unit to reduce the number of metal contacts to only one pair to give four operational levels. Numerical simulation shows that this method can be easily extended to 1×2 programmable units. However, 2×2 programmable units based on the same method show a very high loss in the intermediate levels. We model the PM-TDCs both analytically and numerically to unveil that it is the fundamental wave dynamics in coupled-WG systems that cause a combination of material absorption loss (type I) and radiation loss at the end of the transition WG (type II). In a PM-TDC design, one of the two types of loss presents intermediate states, incurring high optical loss. A modified structure, termed here as phase-detuned three-WG directional coupler (PD-TDC), is proposed to mitigate both types of loss, where the center transition WG is deliberately phase-detuned from the other two WGs for a-GST. By programming the GST patches, we numerically show a three-level 2×2 programmable unit with low insertion loss (IL; $\sim 1.2 \text{ dB}$). Our work provides a new design methodology for programmable photonic devices using lossy PCMs or any other modulation mechanism.

2 Deterministic Multilevel Scheme Using Individually Controlled GST Segments

Figure 1 shows our scheme to achieve deterministic multilevel operation using the binary phase transition of PCM. Instead of engineering the electrical pulse conditions,^{21,22} we propose to individually control multiple segments of GST thin films on silicon WGs to either fully a or c phase using multiple PIN diode heaters with opposite polarity.^{13,33} By programming the state of each GST segment, multiple operation levels can be obtained.

3 Experimental Demonstration of Multilevel 1×1 Programmable Units with Two Unequal Segments

A multilevel 1×1 WG programmable unit can be implemented for either amplitude or phase modulation, depending on whether the PCM is lossy in the c phase. At the telecommunication wavelength of 1550 nm, GST,¹⁹ $\text{Ge}_2\text{Sb}_2\text{Se}_5$,³⁴ or $\text{Ge}_2\text{Sb}_2\text{Se}_4\text{Te}_1$ ³⁵ can be used for amplitude modulation, and Sb_2Se_3 ^{22,23} or Sb_2S_3 ^{21,26,36} can realize phase-only modulation. In the design in Fig. 1(a), each GST segment represents 1 bit, and a device with N segments can present 2^N bits at most. This can be achieved by designing the lengths of GST segment i twice that of segment $i - 1$, see the bottom right sketch in Fig. 1. We note that, in general, unequal segments can generate 2^N levels, but the difference between levels is not the same unless the lengths satisfy the double-length condition.

The rectification behavior of PIN diode heaters can be leveraged to reduce the number of metal wires. Using a series of alternating PIN heaters [Fig. 1(a)], two PIN diode heaters can share the same metal pad because the reversely biased current is small below the breakdown voltage and not enough to trigger any phase transition. Therefore, the number of metal pads can be reduced by half, leading to simplified electrical wire routing. This is beyond the capability of traditional resistive heaters such as the tungsten heater in Ref. 34. Despite controlling two PIN diodes with a single pair of electrodes, one diode remains reverse-biased, resulting in minimal additional current. This current is typically less than $1 \mu\text{A}$, varying with the diode's quality. Such a small extra current guarantees no electromigration on the contact metal. However, the reverse-biased diode and metal could be damaged if the amorphization voltage exceeds the PIN diode's breakdown voltage usually between 10 and 20 V. For PCM-based directional coupler

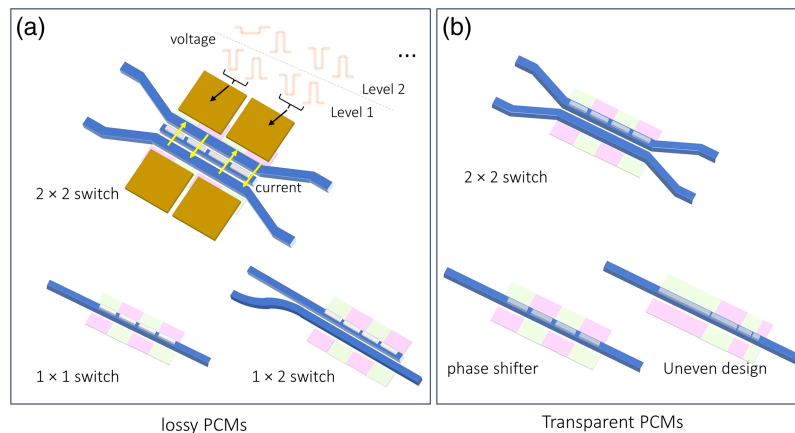


Fig. 1 Our proposed deterministic multilevel programmable units, with multiple PIN diode heaters with reversed polarity to control the phase of each PCM segment in a binary manner: programmable units using (a) lossy and (b) transparent PCMs. Two PIN diodes are controlled by one pair of metals thanks to PIN diode's rectified behavior. Depending on the sign of the applied voltage, a large electric current only occurs on the forward-biased diodes and switches the corresponding PCMs. The reversely biased diode will have limited current; hence, no PCM switching. An example of uneven segment design is shown at the bottom right. We omit the metals in the following pictures to simplify the schematics (colors: pink, p++ doped silicon; green, n++ doped silicon; gold, metal contact; blue, intrinsic silicon; white, lossy PCMs; gray, transparent PCMs).

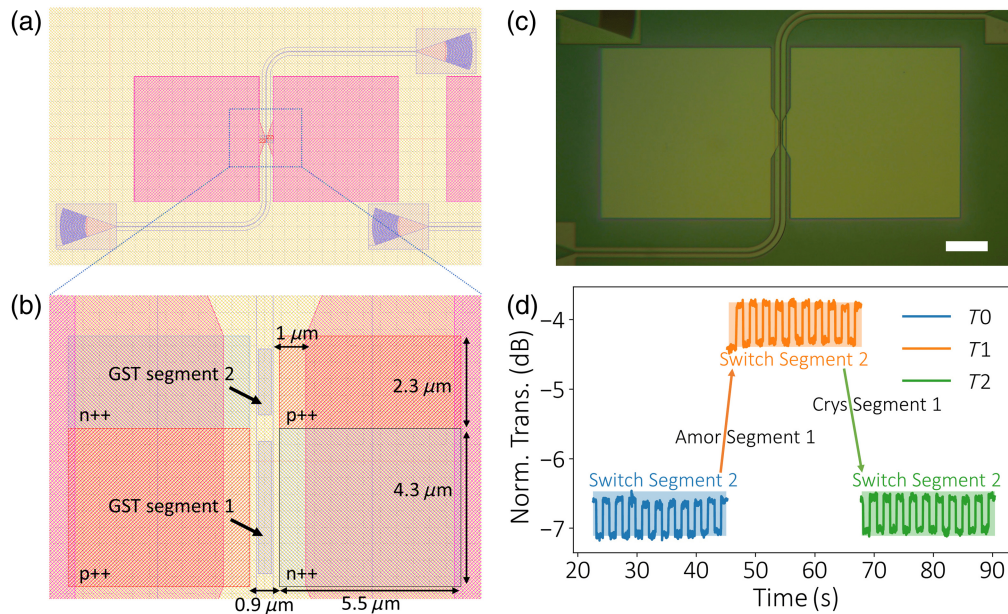


Fig. 2 Deterministic four-level 1×1 programmable unit using two PIN heaters with reversed polarity: (a) schematic of the device; (b) zoomed-in schematic; (c) optical microscope image of the fabricated device, scalebar: $25 \mu\text{m}$; and (d) time-trace measurement, showing four distinct and reversible transmission levels. Measured results for time traces T_0 , T_1 , and T_2 are in blue, orange, and green, respectively, where fine-tuning is achieved in each time trace by switching segment 2 and coarse-tuning is shown between two adjacent time traces by switching segment 1.

switches, a large voltage close to 10 V was used in previous works.^{20,21,28} Therefore, the amorphization pulse must be carefully engineered to use this method.

One potential limitation is the thermal crosstalk between adjacent GST segments. We experimentally show that this thermal crosstalk does not trigger unintentional phase transition by fabricating and characterizing a 1×1 programmable unit. The fabrication process is similar to our previous works.^{20,21,28} We designed the programmable unit with two unequal GST segments (10 nm thick and 2 and $4 \mu\text{m}$ long) and demonstrated four distinct levels. Figure 2 shows the device layout, fabricated devices, and characterization results. The lengths of the PCM patches are engineered [Fig. 2(b)] to provide a maximum number of 2^N states ($N = 2$, therefore four levels). The silicon WGs are 500 nm wide and 220 nm thick without SiO_2 top cladding. The boron- and phosphorus-doping regions have a doping concentration of $\sim 10^{20} \text{ cm}^{-3}$, which are 200 nm away from the WG edge to avoid free-carrier absorption loss. The dimensions of the doping areas are annotated in Fig. 2(b). Metal contacts are formed by $5 \text{ nm}/180 \text{ nm}$ Ti/Pd, which are placed $1 \mu\text{m}$ away from the WG to avoid metal absorption loss. The fabricated device is shown in Fig. 2(c). Time trace sequences in Fig. 2(d) were obtained by recording the transmission at 1550 nm while alternatively applying amorphization (4 V , 100 ns) and crystallization pulses (1.4 V , $50 \mu\text{s}$) on segment 2. The on-off extinction ratio (ER) is 0.6 dB , working as a high-precision tuning knob. Low-precision tuning (T_0 to T_1 and T_1 to T_2 , on-off ER of $\sim 3 \text{ dB}$) was realized by sending in pulses in a reversed bias to control the longer GST segment 1, with -4.5 V for amorphization and -1.5 V for crystallization. We note the polarity is reversed compared with the longer segment. This result shows that the short and long segments are separately tuned without noticeable thermal crosstalk.

4 Optical Design for Deterministic Multilevel 1×2 Programmable Unit

The experimental result in Sec. 3 validates our deterministic multilevel scheme in the 1×1 programmable unit. In this section, we extend the idea to 1×2 and 2×2 programmable units, which

require phase-only modulation and are building blocks for large-scale programmable PICs. To achieve a low-loss operation, a three-WG directional coupler consisting of GST-loaded silicon (hybrid) WG and bare silicon WG was previously reported.^{20,24,31} When GST is in the a phase, the hybrid WG is designed to phase-match with the bare silicon WGs. Therefore, the input light couples to the cross port. When the GST changes to the c state, due to the large effective index difference, the WGs are phase mismatched. As a result, the light barely couples and stays in the bar port, thus bypassing the high loss of c-GST. We emphasize that achieving multilevel operation using this idea requires extra design considerations since the absorption loss of c-GST limits the available phase sequence of the GST segments.

Figure 3 shows the simulation result for a 1×2 optical programmable unit, for which the design is the same as Ref. 20. One change is that two individually controlled GST segments, instead of one, are used to achieve multilevel operation. The achievable low-loss states are, however, not 2^N as in the 1×1 programmable unit case, but $N + 1$ since any a-GST segment before the c-GST segment results in light coupling to the GST-loaded WG, which then gets completely absorbed by the highly lossy c-GST segments. Our simulation results agree with this intuition. We denote the phase sequence from left to right as {phase of segment 1, phase of segment 2} and show the electric field distribution and the transmission spectrum for all four possible phase sequences. Figure 3(b) shows that sequence {a, c} exhibits a high IL of ~ 3 dB due to high absorption of the c-GST segment 2. This is verified by the electric field distribution image, where the light first couples into the cross port along the a-GST segment 1 and then gets completely absorbed by c-GST segment 2. Since the length of the first segment is half of the

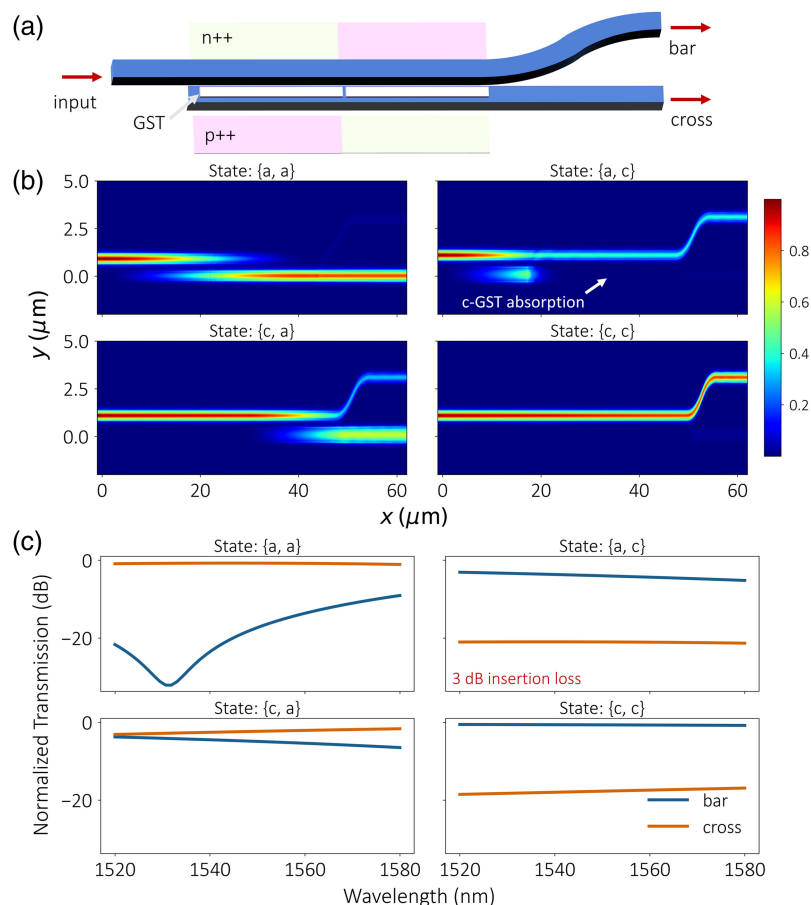


Fig. 3 FDTD simulation for a deterministic three-level 1×2 programmable unit using GST: (a) schematic, (b) intensity distribution, and (c) the corresponding transmission spectra for different GST phase combinations. GST sequence {a, c} introduces an IL of ~ 3 dB due to c-GST absorption loss, pointed by a white arrow in the field distribution map.

coupling length, exactly half of the light is coupled and absorbed, agreeing well with the simulation.

5 Optical Design for Deterministic Multilevel 2×2 Programmable Unit

Previous GST-based low-loss 2×2 programmable units leveraged a PM-TDC structure to circumvent the loss of c-GST.^{20,24,31} In these works, an extra transition WG is placed between two silicon WGs with 20-nm-thick GST deposited on top for active switching. When the GST is in the a phase, the transition WG is designed to phase-match with the other two WGs. Therefore, the input light can be coupled into the transition WG and then to the cross port. On the contrary, once switching the GST to the c phase, a large effective index difference is introduced, and the light can barely couple to the high loss transition WG. This bypasses the high loss of c-GST. Unfortunately, a straightforward extension of this PM-TDC method to multilevel operation does not work as we will show in the following analysis.

5.1 Challenges of Multiple Segments Switching Using the PM-TDC Approach

Figure 4 shows a simulation using a similar design to Ref. 20 but with two GST segments. It shows that both {a, c} and {c, a} phase sequences have a high loss of ~ 3 dB. The former can be explained based on the same concept as in the 1×2 programmable unit case: no c-GST should be placed after an a-GST segment when finite light is still in the transition WG, defined as the type I absorption loss. Besides, the transition WG, which is open at the end, adds another constraint for low-loss operation: no light can remain in the transition WG at the end of this transition WG. Otherwise, that portion of light will radiate and get lost, defined as type II radiation loss.

5.2 Analytical and Numerical Study of the Three-WG Directional Coupler Systems

To tackle this loss issue, it is crucial to understand the intensity dynamics inside of each WG in this coupled WG system. We describe the coupled three-WG system using the following coupled partial differential equation:³⁷

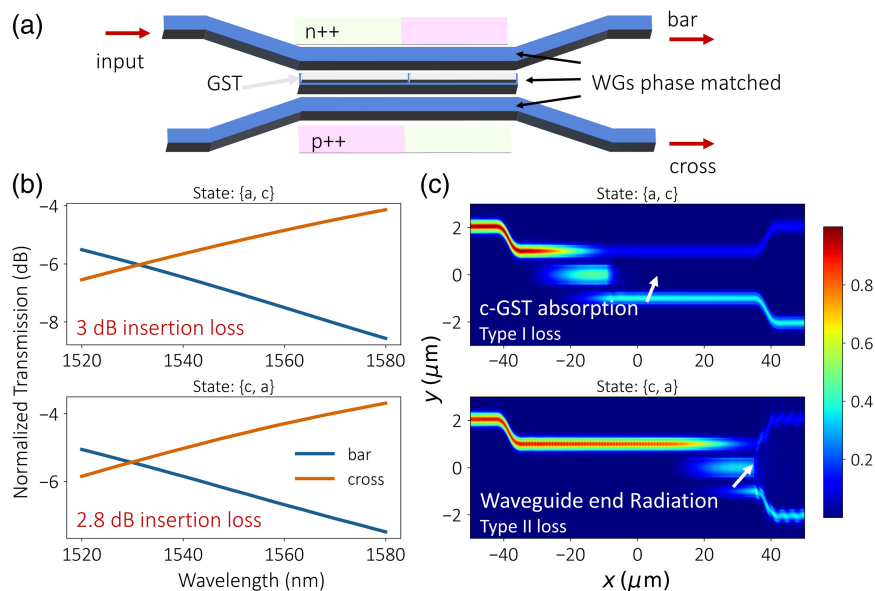


Fig. 4 Phase-matched three-WG 2×2 directional couplers have a high loss for intermediate levels: (a) schematic, (b) the transmission spectra for different GST phase sequences, and (c) the corresponding intensity distribution. Both sequences {a, c} and {c, a} introduce an IL of ~ 3 dB. The former is due to c-GST absorption loss (type I loss), while the latter is due to the radiation loss at the end of the transition WG (type II loss), both indicated by white arrows.

$$\begin{cases} \frac{da_0}{dz} = i\kappa^*(a_1 + a_2) \\ \frac{da_1}{dz} = i\kappa a_0 - i\delta a_1 \\ \frac{da_2}{dz} = i\kappa a_0 - i\delta a_2, \end{cases} \quad (1)$$

where z is the distance in the light propagation direction, $a_{i,i=0,1,2}$ is the amplitude in three WGs in Fig. 5(a), $\kappa = \Delta n_{\text{eff},c} \cdot \frac{2\pi}{\lambda_0}$ and $\delta = \Delta n_{\text{eff},i} \cdot \frac{2\pi}{\lambda_0}$ are the coupling coefficient and detuning between the center and other WGs, $\Delta n_{\text{eff},c}$ is the effective index difference between the supermodes formed by coupled WG0 and WG1 (or WG2), $\Delta n_{\text{eff},i}$ is the effective index difference between the modes in WG0 and WG1 (or WG2) assuming they are isolated, and λ_0 is the vacuum wavelength of light. We note that only the nearest coupling is considered in this model, which is usually a valid assumption in a two-dimensional photonic WG array. We also assume that WG1 and WG2 have the same geometry to simplify the model and neglect the loss term for simplicity. We note that this coupled equation is analytically solvable, see Appendix A. To quickly capture the physics, we show the numerical analysis below.

First, to analyze the case where WG0 is phase-matched with WG1 and WG2, we set δ to zero and solve this equation numerically. We found that the middle WG intensity is zero only when the light is completely in the cross or bar port [Fig. 5(b)]. Therefore, type I loss occurs in the {a, c} state, while type II loss occurs in the {c, a} state. Therefore, we summarize the requirements for low-loss multilevel operation in a three-WG directional coupler as (1) no light can be in the middle WG at a c-GST segment to avoid type-I loss, (2) no light can be at the end of the middle WG to avoid type-II loss, and (3) there must exist some intermediate splitting ratios (except from complete bar or cross) when the intensity of light in WG0 is zero. Obviously, the last requirement can never be fulfilled in a PM-TDC.

5.3 New Degree of Freedom: PD-TDCs

To solve this issue, a new degree of freedom must be introduced. We deliberately designed WG0 to have a phase detuning δ with WG1 and WG2, i.e., a phase-detuned TDC scheme. The phase detuning between WGs can be quantitatively represented by the detuning rate δ , where $\beta = 2\pi/\lambda$ is the vacuum wavevector and Δn_{eff} is the effective index difference between WGs. To intuitively understand the wave dynamics in this system, we performed a numerical simulation as shown in

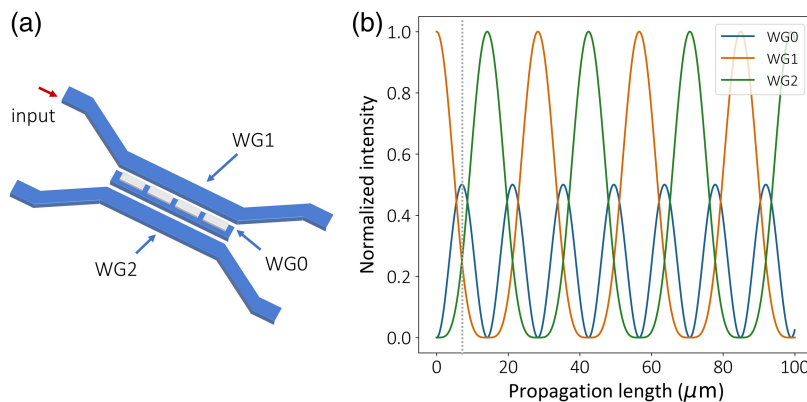


Fig. 5 Analytical model reveals that phase-matched three-WG couplers can never have low-loss intermediate levels: (a) schematic for a generic GST three-WG coupler. The GST patches are denoted in white. In all the discussions, we assume that the WG1 is the input port. (b) Numerically calculated light intensity in three WGs. Blue, orange, and green colors denote WG0, WG1, and WG2, respectively. In the case of two GST segments, phase sequence {c, a} would lead to a propagation distance of $L_c/2$, indicated by the gray dotted line. It is clear that finite energy remains in WG0, causing type II radiative loss.

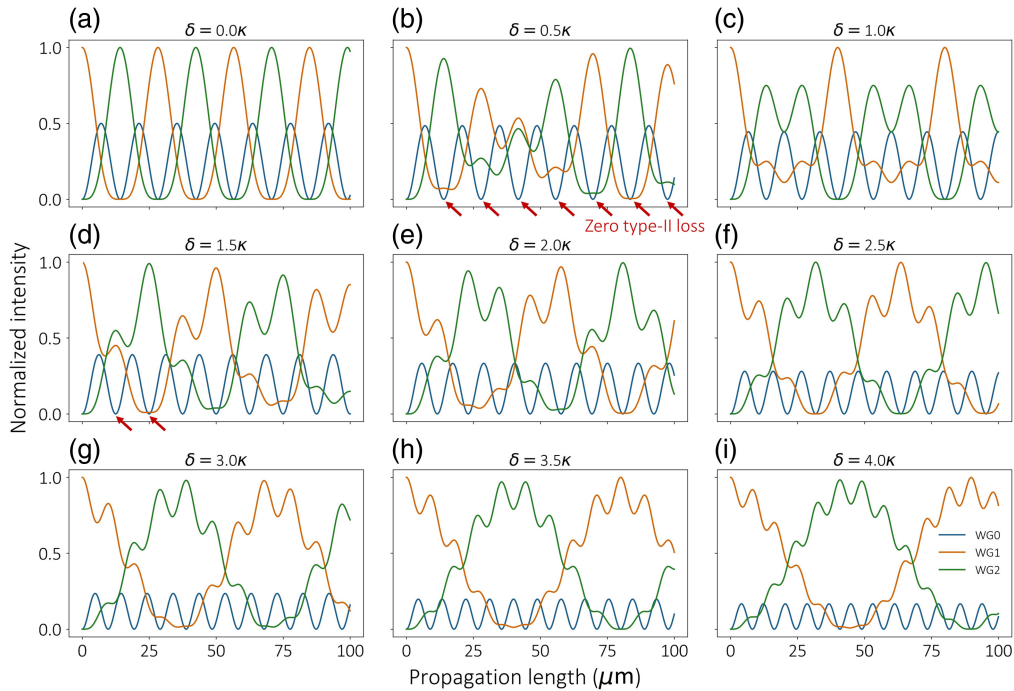


Fig. 6 Detuning the middle WG provides rich optical intensity dynamics, enabling low-loss intermediate levels: (a)–(i) intensity dynamics in the three WGs as the detuning δ varies from 0 to 4κ . As the detuning gets larger, the intensity in WG0 becomes smaller, and that in the other two is smoother. As δ increases from zero, multiple zeros in the blue curve emerge (e.g., pointed by red arrows in panel (b)), overcoming type II loss. Note that this simulation assumes a coupling length L_c of $10 \mu\text{m}$ between WG0 and WG1 (or WG2) when $\delta = 0$.

Fig. 6, where different plots show the intensity in the three WGs versus propagation length under different detuning rates δ . It can be clearly seen that different splitting ratios between WG1 and WG2 can be obtained when zero light is in WG0. We note that Eq. (1) is analytically solvable, and the solution is presented in Appendix A. Another possible solution emerging from this wave dynamics is adding a tapered structure at the end of WG0, which is discussed in more detail in Appendix B.

A tradeoff must be considered when choosing detuning rate δ . A large detuning δ generally creates more zeros in the middle WG within the same coupling region length, hence more achievable intermediate levels. However, a large δ also leads to a longer device (for complete power transfer to the cross port) and hence larger overall loss when GST is in the c phase. To compensate for this, a thicker GST can be used to provide a larger Δn . However, the loss due to a-GST also increases. Furthermore, this makes reversible electrical switching more difficult.

5.4 Design Example of Nonvolatile Multilevel 2×2 Programmable Units Based on GST

Based on the above discussion, we choose $\delta = 1.5\kappa$ and design a multilevel 2×2 programmable unit with an ellipsometry measured GST refractive index (see Appendix B for detailed design procedures). Figure 7 shows the finite-difference time-domain (FDTD) simulation results with a low IL (~ 1.2 dB) and three achievable splitting ratios of 100:0, 50:50, and 0:100. The designed parameters are summarized in Table 1.

Figure 8 shows the IL and ER of the optimized 2×2 programmable unit. The IL is low (~ 1.2 dB) across a broad wavelength (60 nm) for all three levels (four configurations). We emphasize that this IL is mainly due to the relatively thick GST film used in the design, which introduces absorption loss in its a state. By replacing GST with lower loss PCMs such as GSST, we can potentially further reduce the loss. However, the index contrast Δn of GSST is much smaller than GST, which may result in a thicker PCM and longer devices. The ERs of the

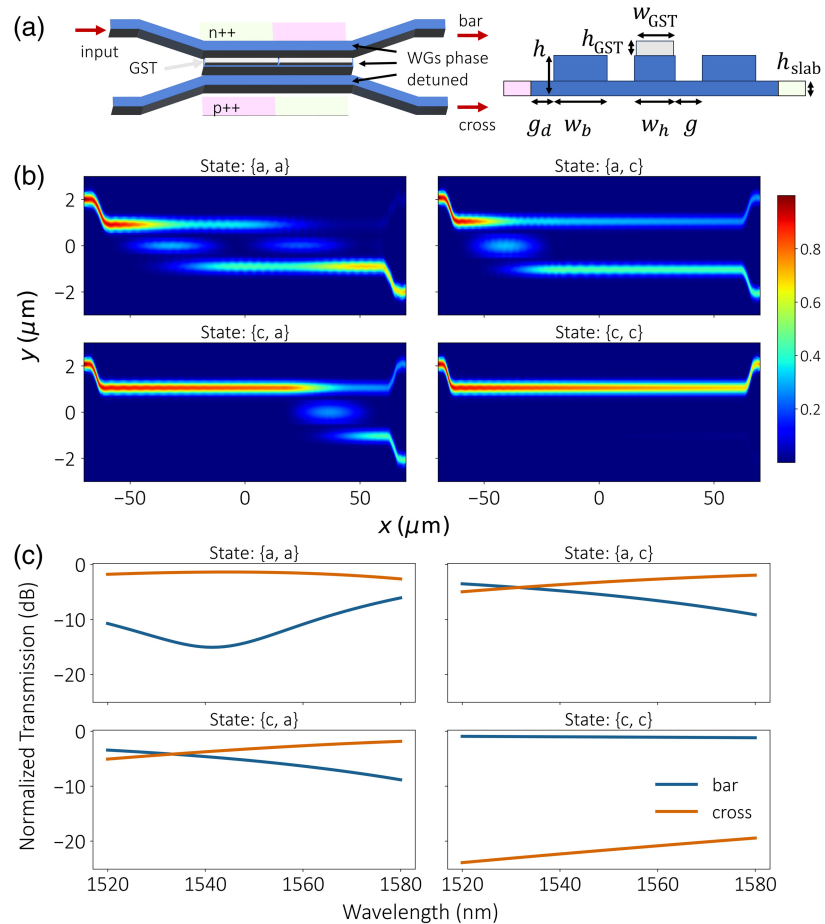


Fig. 7 Optimized deterministic three-level 2×2 programmable units with phase-detuned TDC design ($\delta = 1.5\kappa$): (a) schematic (left) and the cross-sectional view (right). Designed geometry parameters are listed in Table 1. (b) Simulated intensity distribution and (c) the corresponding transmission spectra for different GST phase sequences. The IL is reduced to ~ 1.2 dB compared with ~ 3 dB in traditional PM-TDC designs.

Table 1 Designed parameters for the multilevel 2×2 GST programmable unit with $\delta = 1.5\kappa$.

h (nm)	h_{slab} (nm)	g_d (nm)	w_b (nm)	w_h (nm)	g (nm)	h_{GST} (nm)	w_{GST} (nm)	l_c (μm)
220	100	200	630	500	315	30	450	115

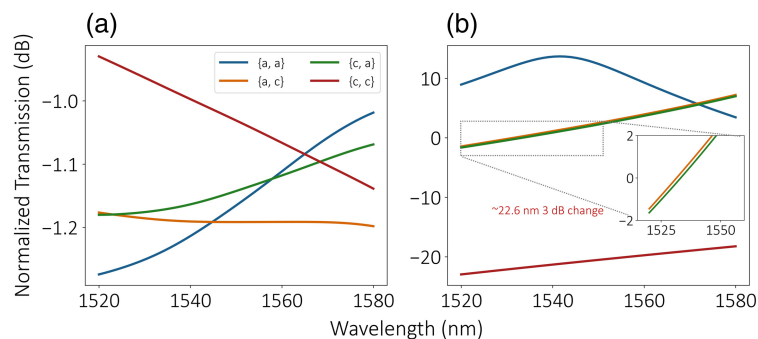


Fig. 8 Simulated transmission spectrum of the designed three-level 2×2 TDC programmable unit ($\delta = 1.5\kappa$): The device shows (a) a low loss (< 1.2 dB) for all four GST sequences and (b) a bandwidth of ~ 22.6 nm with less than 3 dB ER variation.

complete cross and bar states remain high across 60 nm, but the intermediate states are more wavelength-sensitive with a 3 dB variation bandwidth of ~ 22.6 nm.

6 Discussion

The number of operation levels of our device is determined by the phase detuning δ and by the wave dynamics of the three-WG system. From Fig. 6, an arbitrary number of levels can be achieved if the detuning δ is large enough, which, however, incurs a long device length. Moreover, a-GST has finite absorption loss at 1550 nm, and a longer device leads to not only limited device density but also a larger IL. In the future, the number of operation levels can be improved using other PCMs with zero loss in the a phase, such as GSST. Another approach is to add a tapered structure at the end of the middle WG, which forces light to transfer completely to the other two WGs, see Appendix B. However, both approaches would cause a longer device, limiting the integration density of the system.

Using transparent PCMs, such as Sb_2Se_3 and Sb_2S_3 , we can easily extend the multilevel design to a 2×2 programmable unit.^{21,38} The design principle is similar, and the switching of output ports relies on the effective index change of the hybrid WG when the PCM is switched. Importantly, since transparent PCMs introduce negligible excess loss, 2^N distinguished splitting ratios can be easily achieved by varying PCM segment lengths.³³ This is a result of the reduced design complexity due to the relaxed loss requirements. Table 2 summarizes some recent results of broadband 2×2 multilevel switches using transparent PCMs in terms of IL, PCM length, number of levels, number of electrodes, and whether the devices support deterministic multilevel operation. Notably, Ref. 39 showed that c-GST exhibits an unacceptable absorption loss when directly used for phase modulation in a Mach–Zehnder interferometer. Unsurprisingly, transparent PCMs show lower IL, a higher number of levels, and a smaller number of electrodes. However, these transparent PCMs are more challenging to be integrated into photonic foundries for high-volume production.

In summary, we have numerically demonstrated GST-based silicon photonic programmable units with low IL and deterministic multilevel. The multilevel operation is achieved via a novel design where interleaved PIN silicon heaters separately control each GST segment. By programming each GST segment's phase, deterministic multilevel operations are obtained. To demonstrate that the thermal crosstalk does not introduce unwanted PCM phase transition, we fabricated and characterized a two-GST-segment, four-level 1×1 programmable unit. The experimental result shows four distinct transmission levels, and each level is accessible, reliable, and reversible. Based on this idea, we also designed 1×2 and 2×2 programmable units with low IL. A phase-detuned TDC geometry was proposed to achieve a low-loss 2×2 programmable unit, and we numerically demonstrated a design with a low IL (~ 1.2 dB) and three operation levels. This novel design idea provides a way to achieve low-loss photonic switches with multiple operation levels using lossy tuning media.

Table 2 Comparing multilevel 2×2 switches based on lossy and transparent PCMs.

Ref.	Year	PCM	Structure	IL (dB)	PCM length (μm)	Number of levels	Number of electrode pairs	Deterministic multilevel
23	2021	Sb_2Se_3	MZI ^a	>0.3	11	8	1	No
39	2023	GST	MZI ^a 1×2	1 (15) ^b	10	64	1	No
21	2023	Sb_2S_3	DC ^a	<1	79	32	1	No
33	2023	Sb_2S_3	MZI ^a	~ 1	105	8	3	Yes
This work	2024	GST	DC ^a	~ 1.2	115	3	1	Yes

Note: here, only devices with reversible switching are compared.

^aThis work contains multiple devices; only one device is picked for easy comparison.

^bThe IL for a- and c-GST (IL, insertion loss; MZI, Mach–Zehnder interferometer; DC, directional coupler).

7 Appendix A: Low-Loss Multilevel 2×2 GST Programmable Unit Design Procedure

7.1 Analytical Solution to Eq. (1)

Equation (1) is analytically solvable. The light intensity inside of each WG can be expressed as

$$\begin{cases} I_0(z) = \frac{1}{\left(\frac{\delta}{2\kappa}\right)^2 + 2} \left[1 - \frac{\cos(\sqrt{\Delta}z)}{2} \right] \\ I_1(z) = \frac{1}{4} \left[1 + \frac{4\kappa^2 + \delta^2}{\Delta} + \frac{\sqrt{\Delta} - \delta}{\sqrt{\Delta}} \cos(\beta_{12}z) - \frac{\sqrt{\Delta} + \delta}{\sqrt{\Delta}} \cos(\beta_{13}z) - \frac{\Delta - \delta^2}{\Delta} \cos(\beta_{23}z) \right] \\ I_2(z) = \frac{1}{4} \left[1 + \frac{4\kappa^2 + \delta^2}{\Delta} - \frac{\sqrt{\Delta} - \delta}{\sqrt{\Delta}} \cos(\beta_{12}z) + \frac{\sqrt{\Delta} + \delta}{\sqrt{\Delta}} \cos(\beta_{13}z) - \frac{\Delta - \delta^2}{\Delta} \cos(\beta_{23}z) \right], \end{cases} \quad (2)$$

where $I_i(z)$ is the propagation distance dependent intensity in WG i , $i = 0, 1, 2$ and

$$\begin{cases} \Delta = 8\kappa^2 + \delta^2 \\ \beta_{ij} = \beta_i - \beta_j \\ \beta_1 = -\delta \\ \beta_2 = -\frac{\delta - \sqrt{\Delta}}{2} \\ \beta_3 = -\frac{\delta + \sqrt{\Delta}}{2}, \end{cases} \quad (3)$$

where δ is the detuning, κ is the coupling ratio, and β_i is the propagation constant for the i 'th supermode.

Assume the effective refractive indices for a- and c-GST are n_a and n_c , respectively. The detuning between c- and a-GST, δ_{ca} , is given by

$$\delta_{ca} = \frac{2\pi}{\lambda_0} \cdot (n_c - n_a) = k_0 \cdot dn_{ca}, \quad (4)$$

where $dn_{ca} = n_c - n_a$. Assume $\delta_{ca} = \delta_c - \delta_a = (N - 1)\delta$ and $\delta_a = \delta = M\kappa$, we can write down the following equation:

$$\begin{cases} \kappa = \frac{dn_{ca}}{M(N - 1)} k_0 \\ \delta_a = M\kappa = \frac{dn_{ca}}{N - 1} k_0 \\ \delta_c = N\delta_a = \frac{N \cdot dn_{ca}}{N - 1} k_0 \\ L_0 = \frac{\pi}{2\sqrt{\Delta}} = \frac{M(N - 1)}{4\sqrt{8 + M^2} dn_{ca}} \lambda_0, \end{cases} \quad (5)$$

where L_0 is the coupling length of WG0. The total device length is determined by $2L_0 \times$ (number of levels—1) (as in Fig. 6). For example, if $M = 1.5$, the device length $L_{dev} = 2L_0 \times (3 - 1) = 4L_0$.

7.2 Design Procedures for PD-TWDs

The design procedure can be described as the following steps:

1. Assume an operation wavelength of $\lambda_0 = 1.55 \mu\text{m}$ and standard 220 nm silicon on insulator wafer. The WG is formed by partially etching the silicon by 120 nm. The remaining 100-nm slab is used for doping. Determine suitable constants M and N to achieve reasonable numbers of levels, phase mismatch between a- and c-GST, and device length. Here, we used $M = 1.5$ and $N = 30$ to achieve three operation levels and reasonable ER between a- and c-GST.

- Fix the width of the WG0 (w_h) and PCM thickness (h_{PCM}), such as to $w_h = 500$ nm and $h_{\text{PCM}} = 20$ nm. Then, calculate the effective indices for both a and c phases to determine dn_{ca} . Calculate the desired detuning rate δ_a , coupling coefficient κ from M , N , dn_{ca} , and λ_0 . Estimate the device length L_{dev} . If the device length is too long, increase PCM thickness (h_{PCM}) and repeat this step. Here, we used $h_{\text{PCM}} = 30$ nm to achieve a high refractive index contrast and obtained the following parameters: $\delta_a = 0.04959 \mu\text{m}^{-1}$, $\kappa = 0.03306 \mu\text{m}^{-1}$, and $L_{\text{dev}} = 115 \mu\text{m}$.
- Sweep the width of the bare silicon WG (w_b) to optimize the detuning rate δ_a . We calculated the desired effective index as 2.67177 and optimized $w_b = 630$ nm.
- Sweep the gap to optimize the coupling coefficient κ . We sweep the gap between 300 and 400 nm and obtained the desired κ when it is 315 nm.
- Run an FDTD simulation to verify the field distribution in the WG. Our FDTD results are shown in Figs. 7 and 8.

8 Appendix B: Discussion on Using a Tapered Structure in the Middle WG for Multilevel Switching

The tapered WG structure can usually reduce the loss from mode mismatches when the WG structure changes,²³ which is rarely explored in three-WG systems. In this section, we briefly discuss the potential of using a tapered middle WG in phase-matched three-WG systems to achieve multilevel switching. Figure 9 shows our proposed device, where the middle WG has a taper at the end. The taper can adiabatically guide all the light to the other two WGs to ensure no light remains in the middle WG at the end and hence no type II loss.

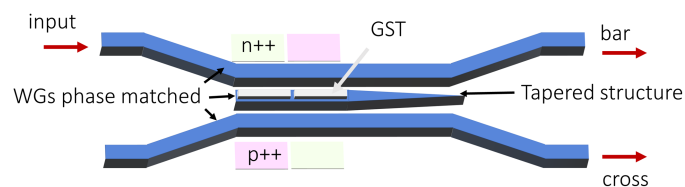


Fig. 9 An alternative design with phase-matched middle WG and a tapered structure at the end of the middle WG. It can potentially enable arbitrary multilevel switching but at the cost of a much longer device.

The rationale of this design can be understood from Fig. 6. The three-WG system with a tapered middle WG has the detuning δ increasing with the propagation length, causing the amplitude in the middle WG to decrease. One can see from Fig. 6 that the wave dynamics in the three-WG system change drastically with δ . To avoid extra mode mismatch loss, detuning δ should vary as slowly as possible, incurring a long coupling region. Such a long coupling distance is quite common for adiabatic directional couplers unless adiabatic mode evolution is carefully engineered.^{40,41} A more detailed study of this structure is already beyond the scope of this paper and may constitute future research directions.

Disclosures

The authors declare that they have no competing interests.

Code and Data Availability

The code for numerically solving the three-WG propagation problem can be found at <https://github.com/charey6/TriWG.git>. All data in support of the findings of this paper are available within the article or in the appendix.

Author Contributions

R.C. and A.M. conceived the project. R.C. simulated the nonvolatile programmable units, fabricated the samples, and performed optical characterizations and data analysis. J.D., V.T., Z.F.,

and J.Z. helped with the design and data analysis. A.M. supervised and planned the project. R.C. wrote the paper with input from all the authors.

Acknowledgments

The research is funded by the National Science Foundation (Grant No. NSF-2003509), ONR-YIP Award, DRAPER Labs, DARPA-YFA Award, and Intel. Part of this work was conducted at the Washington Nanofabrication Facility/Molecular Analysis Facility, a National Nanotechnology Coordinated Infrastructure (NNCI) site at the University of Washington with partial support from the National Science Foundation (Award Nos. NNCI-1542101 and NNCI-2025489).

References

1. W. Bogaerts et al., “Programmable photonic circuits,” *Nature* **586**(7828), 207–216 (2020).
2. Y. Shen et al., “Deep learning with coherent nanophotonic circuits,” *Nat. Photonics* **11**(7), 441–446 (2017).
3. D. Marpaung, J. Yao, and J. Capmany, “Integrated microwave photonics,” *Nat. Photonics* **13**(2), 80–90 (2019).
4. N. C. Harris et al., “Quantum transport simulations in a programmable nanophotonic processor,” *Nat. Photonics* **11**(7), 447–452 (2017).
5. A. Saxena et al., “Realizing tight-binding Hamiltonians using site-controlled coupled cavity arrays,” *Nat. Commun.* **14**(1), 5260 (2023).
6. D. Pérez et al., “Multipurpose silicon photonics signal processor core,” *Nat. Commun.* **8**(1), 636 (2017).
7. W. Zhang and J. Yao, “Photonic integrated field-programmable disk array signal processor,” *Nat. Commun.* **11**(1), 406 (2020).
8. C. Wang et al., “Integrated lithium niobate electro-optic modulators operating at CMOS-compatible voltages,” *Nature* **562**(7725), 101–104 (2018).
9. G. T. Reed et al., “Silicon optical modulators,” *Nat. Photonics* **4**(8), 518–526 (2010).
10. M. R. Watts et al., “Adiabatic thermo-optic Mach–Zehnder switch,” *Opt. Lett.* **38**(5), 733 (2013).
11. S. Abdollahramezani et al., “Tunable nanophotonics enabled by chalcogenide phase-change materials,” *Nanophotonics* **9**(5), 1189–1241 (2020).
12. Z. Fang et al., “Non-volatile reconfigurable silicon photonics based on phase-change materials,” *IEEE J. Sel. Top. Quantum Electron.* **28**(3), 8200317 (2022).
13. R. Chen et al., “Opportunities and challenges for large-scale phase-change material integrated electro-photonics,” *ACS Photonics* **9**(10), 3181–3195 (2022).
14. N. Youngblood et al., “Integrated optical memristors,” *Nat. Photonics* **17**(7), 561–572 (2023).
15. C. Rios et al., “Integrated all-photonic non-volatile multi-level memory,” *Nat. Photonics* **9**(11), 725–732 (2015).
16. J. Zheng et al., “GST-on-silicon hybrid nanophotonic integrated circuits: a non-volatile quasi-continuously reprogrammable platform,” *Opt. Mater. Express* **8**(6), 1551 (2018).
17. C. Wu et al., “Low-loss integrated photonic switch using subwavelength patterned phase change material,” *ACS Photonics* **6**(1), 87–92 (2019).
18. C. Wu et al., “Programmable phase-change metasurfaces on waveguides for multimode photonic convolutional neural network,” *Nat. Commun.* **12**(1), 96 (2021).
19. J. Zheng et al., “Nonvolatile electrically reconfigurable integrated photonic switch enabled by a silicon PIN diode heater,” *Adv. Mater.* **32**(31), 2001218 (2020).
20. R. Chen et al., “Broadband nonvolatile electrically controlled programmable units in silicon photonics,” *ACS Photonics* **9**(6), 2142–2150 (2022).
21. R. Chen et al., “Non-volatile electrically programmable integrated photonics with a 5-bit operation,” *Nat. Commun.* **14**(1), 3465 (2023).
22. Z. Fang et al., “Ultra-low-energy programmable non-volatile silicon photonics based on phase-change materials with graphene heaters,” *Nat. Nanotechnol.* **17**(8), 842–848 (2022).
23. C. Ríos et al., “Ultra-compact nonvolatile phase shifter based on electrically reprogrammable transparent phase change materials,” *PhotonIX* **3**(1), 26 (2022).
24. P. Xu et al., “Low-loss and broadband nonvolatile phase-change directional coupler switches,” *ACS Photonics* **6**(2), 553–557 (2019).
25. M. Delaney et al., “A new family of ultralow loss reversible phase-change materials for photonic integrated circuits: Sb₂S₃ and Sb₂Se₃,” *Adv. Funct. Mater.* **30**(36), 2002447 (2020).
26. Z. Fang et al., “Non-volatile reconfigurable integrated photonics enabled by broadband low-loss phase change material,” *Adv. Opt. Mater.* **9**, 2002049 (2021).
27. W. Dong et al., “Wide bandgap phase change material tuned visible photonics,” *Adv. Funct. Mater.* **29**(6), 1806181 (2019).

28. Z. Fang et al., "Arbitrary programming of racetrack resonators using low-loss phase-change material Sb_2Se_3 ," *Nano Lett.* **24**(1), 97–103 (2023).
29. S. Kim et al., "Phase-change memory cycling endurance," *MRS Bull.* **44**(9), 710–714 (2019).
30. S. Hudgens and B. Johnson, "Overview of phase-change chalcogenide nonvolatile memory technology," *MRS Bull.* **29**(11), 829–832 (2004).
31. Q. Zhang et al., "Broadband nonvolatile photonic switching based on optical phase change materials: beyond the classical figure-of-merit," *Opt. Lett.* **43**(1), 94 (2018).
32. T. Tuma et al., "Stochastic phase-change neurons," *Nat. Nanotechnol.* **11**(8), 693–699 (2016).
33. R. Chen et al., "Deterministic quasi-continuous tuning of phase-change material integrated on a high-volume 300-mm silicon photonics platform," preprint (Version 1), in review (2023).
34. J. Meng et al., "Electrical programmable multilevel nonvolatile photonic random-access memory," *Light Sci. Appl.* **12**(1), 189 (2023).
35. Y. Zhang et al., "Broadband transparent optical phase change materials for high-performance nonvolatile photonics," *Nat. Commun.* **10**(1), 4279 (2019).
36. X. Yang et al., "Phase change material enabled 2×2 silicon nonvolatile optical switch," *Opt. Lett.* **46**(17), 4224–4227 (2021).
37. Y. Chen, S.-T. Ho, and V. Krishnamurthy, "All-optical switching in a symmetric three-waveguide coupler with phase-mismatched absorptive central waveguide," *Appl. Opt.* **52**(36), 8845 (2013).
38. T. Y. Teo et al., "Comparison and analysis of phase change materials-based reconfigurable silicon photonic directional couplers," *Opt. Mater. Express* **12**(2), 606–621 (2022).
39. C. Zhang et al., "Nonvolatile multilevel switching of silicon photonic devices with $\text{In}_2\text{O}_3/\text{GST}$ segmented structures," *Adv. Opt. Mater.* **11**(8), 2202748 (2023).
40. J. M. F. Cabanillas and M. A. Popovic, "Fast adiabatic mode evolution based on geometry-induced suppression of nearest-mode crosstalk," in *Conf. Lasers and Electro-Opt., CLEO 2018 – Proc.*, Vol. 1(c), pp. 5–6 (2018).
41. Y.-J. Hung et al., "Mode-evolution-based silicon-on-insulator 3 dB coupler using fast quasiadiabatic dynamics," *Opt. Lett.* **44**(4), 815 (2019).

Rui Chen is a fourth year graduate student at the University of Washington, working with Prof. Arka Majumdar. He received his bachelor's degree from Zhejiang University in 2018 and his MS degree from Columbia University in 2020. His main research interests include phase-change material-based reconfigurable photonic integrated circuits and programmable metasurfaces.

Arka Majumdar is an associate professor in the Departments of Electrical and Computer Engineering and Physics, University of Washington. He received his BTech degree from IIT-Kharagpur in 2007, where he was honored with the President's Gold Medal. He completed his MS and PhD degrees in electrical engineering at Stanford University in 2009 and 2012, respectively. He spent one year at the University of California, Berkeley, in 2012–2013 as a postdoc before joining Intel Labs in 2013–2014. His research interest includes developing a hybrid nanophotonic platform using emerging material systems for optical information science, imaging, and microscopy.

Biographies of the other authors are not available.